Estimating Microphysics Properties in Ice-Dominated Clouds from Airborne Ka–W-band Dual-Wavelength Ratio Reflectivity Factor in Close Proximity to In Situ Probes

COLTIN GRASMICK,[a] BART GEERTS,[a] JEFFREY R. FRENCH,[a] SAMUEL HAIMOV,[a] AND ROBERT M. RAUBER[b]

[a] *Department of Atmospheric Sciences, University of Wyoming, Laramie, Wyoming*
[b] *Department of Atmospheric Sciences, University of Illinois at Urbana–Champaign, Urbana, Illinois*

(Manuscript received 4 October 2021, in final form 18 July 2022)

ABSTRACT: Properties of frozen hydrometeors in clouds remain difficult to sense remotely. Estimates of number concentration, distribution shape, ice particle density, and ice water content are essential for connecting cloud processes to surface precipitation. Progress has been made with dual-frequency radars, but validation has been difficult because of lack of particle imaging and sizing observations collocated with the radar measurements. Here, data are used from two airborne profiling (up and down) radars, the W-band Wyoming Cloud Radar and the Ka-band Profiling Radar, allowing for Ka–W-band dual-wavelength ratio (DWR) profiles. The aircraft (the University of Wyoming King Air) also carried a suite of in situ cloud and precipitation probes. This arrangement is optimal for relating the "flight-level" DWR (an average from radar gates below and above flight level) to ice particle size distributions measured by in situ optical array probes, as well as bulk properties such as minimum snow particle density and ice water content. This comparison reveals a strong relationship between DWR and the ice particle median-volume diameter. An optimal range of DWR values ensures the highest retrieval confidence, bounded by the radars' relative calibration and DWR saturation, found here to be about 2.5–7.5 dB. The DWR-defined size distribution shape is used with a Mie scattering model and an experimental mass–diameter relationship to test retrievals of ice particle concentration and ice water content. Comparison with flight-level cloud-probe data indicate good performance, allowing microphysical interpretations for the rest of the vertical radar transects.

KEYWORDS: Complex terrain; Cloud microphysics; Drop size distribution; Aircraft observations; Radars/Radar observations; Remote sensing

1. Introduction

The use of remote sensing to diagnose cloud microphysics and, ultimately, quantify parameters such as cloud radiative transfer or surface precipitation, may be improved through proper identification of hydrometeor phase, size, shape, and concentration. Ice hydrometeors are particularly difficult to characterize due to additional variations of shape and effective density, which may vary across cloud types and even within a single cloud (Field 1999; Heymsfield et al. 2004; McFarquhar et al. 2007). Such variability makes relationships between mass and size unreliable because a single mass–diameter relationship cannot be applied consistently when crystal habit is constantly evolving (Finlon et al. 2019). For this reason, the ability to derive a scatterers' mass, size, and or density characteristics along the radar beam is especially useful. Differences in the power and phase of the returned radar signal at multiple polarizations can help identify different populations of hydrometeors based on intrinsic properties such as shape and mass (e.g., Thompson et al. 2014). Dual-pol measurements allow improved particle identification and quantitative precipitation estimation (e.g., Kumjian 2013). This led to widespread use, including for operational radars such as the S-band NEXRAD network (e.g., Ryzhkov et al. 2005). However, dual-pol hydrometeor identification schemes determine discrete, best-guess hydrometeor types, but not their size distribution. This approach causes information to be lost in transition zones or volumes with multiple hydrometeor types. In addition, they require additional hardware and space, which is often not available on airborne, spaceborne, or other agile platforms (Rauber and Nesbitt 2018, chapter 2.3).

Dual-wavelength radars can use an alternate approach to estimate characteristics of hydrometeors. Dual- or multiple-wavelength equivalent reflectivity factor (hereafter, reflectivity) does not provide information on the type of scatterers (e.g., insects, rain, snow, graupel), but provides insights into particle size distribution and, in some situations, cloud liquid water content (e.g., Hogan et al. 2005). These applications are possible using a few short-wavelength radars, which can be made quite small and installed on an aircraft or a satellite. The focus here is on mm-wave radars.

The difference in reflectivity between the different-wavelength radars is called the *dual-wavelength ratio* (DWR; or dual-frequency ratio, expressed in dB units), which becomes larger in magnitude as scattering and absorption (or attenuation) affects one radar wavelength more than the other one (Rauber and Nesbitt 2018, chapter 17.2). For clouds that are composed primarily of ice, like those investigated in this study, liquid attenuation is small such that the DWR can be related to the scattering properties of particles within the same contributing volume. When particles are much smaller than both wavelengths, Rayleigh scattering occurs and the microwave scattering by the particles is expected to be similar for both wavelengths. If the contributing volume contains particles whose equivalent diameter becomes a significant fraction of the transmitted wavelengths, reflectivity no longer increases exponentially with particle diameter but

---

Corresponding author: Coltin Grasmick, cgrasmic@uwyo.edu

DOI: 10.1175/JTECH-D-21-0147.1

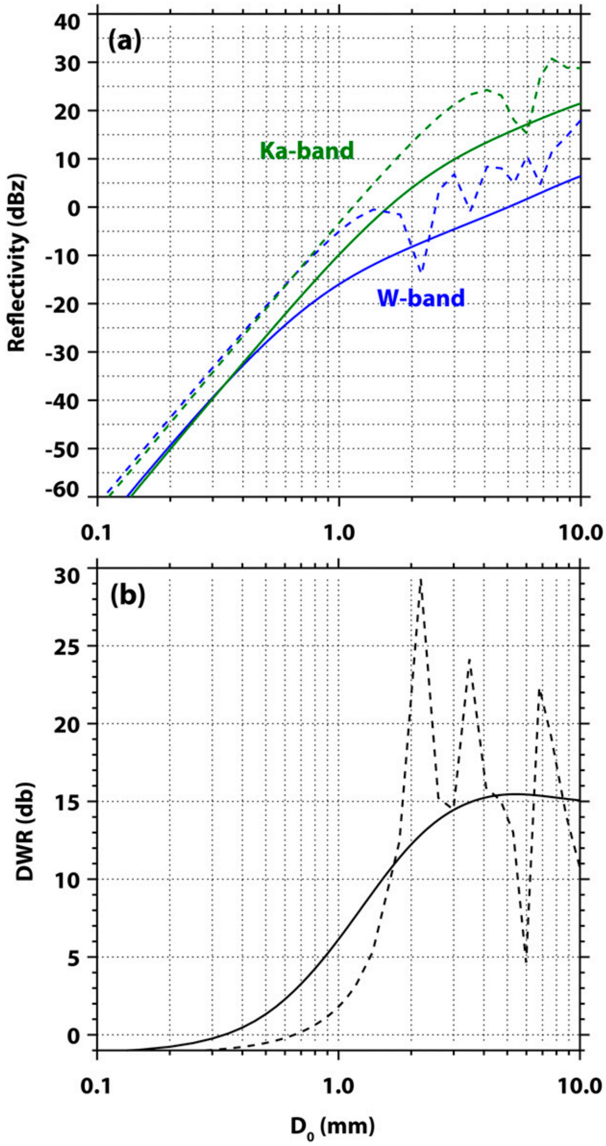

FIG. 1. (a) Theoretical reflectivity for W- and Ka-band radars [blue and green lines, respectively, in (a)] and (b) the resulting DWR as a function of the median-volume diameter (D_0). Mie calculations assume spherical snow particles with density 0.1 g m^{-3} and concentrations of 3 L^{-1}. Dashed lines are for a monodisperse particle population. Solid lines are for a gamma size distribution defined by its median-volume diameter and an exponential distribution (shape parameter = 0).

oscillates with further increases of particle diameter (Fig. 1). Within this Mie regime, radars of different wavelengths will produce different reflectivity values. This difference can be exploited to estimate size of particles producing the observed backscatter (e.g., Matrosov 1992, 1998; Vivekanandan et al. 2001; Liao et al. 2005).

The viability of dual, or triple, wavelength algorithms for ice microphysics retrievals is becoming more apparent thanks to recent observational experiments (e.g., Wang et al. 2005; Kneifel et al. 2015; Grecu et al. 2018; Duffy et al. 2021) and theoretical/modeling work (e.g., Kneifel et al. 2011; Hogan et al. 2012; Leinonen et al. 2013). In most applications, one or more DWRs are related to a scattering population's effective crystal size and/or bulk density, both of which are associated with crystal habit. The effective crystal size provides information about the particle size distribution (PSD), specifically about the number of larger (Mie regime) particles. After assuming a shape to the PSD (typically an exponential or gamma distribution), a forward calculation of reflectivity using a scattering model can provide an estimate of number concentration. The greatest limitation seems to be in ice scattering models; various models and approximations exist, but none consistently reproduce all the observed double- or triple-wavelength signatures (Kneifel et al. 2015; Tridon et al. 2019).

Most ground-based and spaceborne dual- and triple-frequency studies have been hampered by lack of representative in situ observations of hydrometeor properties. Achieving collocated radar and microphysics observations (collected aboard two separate vertically stacked aircraft) often requires nearest-neighbor algorithms with disparity in time and space on the order of minutes and kilometers (e.g., Wang et al. 2005; Duffy et al. 2021). Here, we use the W-band (94.9 GHz–3.2 mm wavelength) Wyoming Cloud Radar (WCR) and the Ka-band (35.6 GHz–8.4 mm wavelength) Precipitation Radar (KPR) aboard the University of Wyoming King Air (UWKA). Both radars are profiling, above and below the aircraft. An averaging or interpolation of reflectivity values in the first gate(s) starting at about 120 m above and below flight level provides a "flight-level" estimation (i.e., centered at flight level), for comparison against in situ sizing and imaging probes. Because the microphysical and DWR observations are from the same platform, the disparity in time and space are small. Collocated data are matched in time to the nearest second and the flight-level estimation improves upon the true distance, which is on the order of 100 m.

Previous studies using the Ka- and W-band radars have shown a direct relationship between mass- (or volume-) weighted ice diameter and the Ka–W DWR (Hogan et al. 2005; Kneifel et al. 2015; Chase et al. 2018). There are some inconsistencies for the relationship between this DWR and bulk ice density, possibly caused by the amount of riming. Kneifel et al. (2015) observed greater ice density for increases in Ka–W DWR and modeling by Leinonen and Szyrmer (2015) attribute this to additional non-Rayleigh scattering from riming of aggregates. Chase et al. (2018) observed one case where bulk density clearly covaried with Ka–W DWR. Hogan et al. (2000) used the Ka–W DWR to estimate crystal size and ice water content (IWC) in cirrus clouds using a scattering model. While ice crystals in cirrus clouds are typically small, they demonstrated the DWR's potential for sizing crystals down to around 200 μm although they lacked aircraft measurements for validation and showed that variations in density could bias the results. Mason et al. (2018) made progress toward retrieving bulk snow density by using a ground-based Ka–W DWR within an optimal estimation framework. Their experiments comparing retrievals to surface observations showed that both

Doppler velocity and the dual-wavelength measurements improve estimations of PSD parameters and bulk ice density.

NASA recognized the value of dual-wavelength measurements and launched the Global Precipitation Measurement (GPM) satellite, with overlapping Ku- and Ka-band (22.1 and 8.5 mm wavelength) radars in 2014 (Hou et al. 2014). The goals of the GPM Dual-Frequency Precipitation Radar (DPR) are to provide better PSD estimates, improve phase identification capabilities, estimate column water content, and correct for attenuation—all ultimately intending to better measure surface precipitation (Hou et al. 2014). Similar applications may be possible using the two radars on the UWKA.

The goal of this study is to investigate the potential for a Ka–W DWR microphysics retrieval algorithm by comparing near-flight-level DWR with airborne in situ observations and the DWR predicted by a simple Mie model. The comparison with observed PSDs will show the range of DWR values sensitive to microphysical changes and the Mie model will reveal whether the variation in DWR is predictable and if further algorithm development is warranted. Section 2 describes the data and observational methods including the matching of radar contributing volumes, aircraft in situ measurements, and the scattering model used to estimate number concentration. Section 3 presents the flight-level comparison between the DWR and hydrometeor properties, followed by the results for a 2D cross section. Section 4 tests the results using a different dataset, then sections 5 and 6 contain the discussion and conclusions.

2. Data and observational methods

a. *The Wyoming Cloud Radar and Ka-band probe radar*

The dataset used in this project is from the Seeded and Natural Orographic Wintertime Clouds: The Idaho Experiment (SNOWIE) campaign (Tessendorf et al. 2019), in which both airborne radars were operational aboard the UWKA for 12 flights in orographic clouds. For the purposes of this project, we use data from two intensive observation periods (IOPs): one for algorithm development (IOP 14) and the other for algorithm testing (IOP 16). SNOWIE IOPs typically lasted about four hours. These IOPs are chosen for their lack of supercooled liquid water and for the quality of in situ measurements of size distributions. Using high-quality PSD data is of the utmost importance in algorithm development and it was deemed better to have a smaller sample size that is robustly quality controlled than a large sample of data with less certain quality. Furthermore, the KPR's Ka-band low noise amplifier had to be repaired two times during the campaign, each time requiring a new calibration. Any resulting shifts in measured reflectivity are unfavorable for our analysis, so we limit our range of IOPs used in this study to a period with no repair of the low noise amplifier.

The WCR is a W-band pulsed Doppler radar with beams pointing above and below the aircraft (Wang et al. 2012). The KPR is a Ka-band Doppler radar, also with up and down pointing beams (Haimov et al. 2018). Reflectivity measured by the longer-wavelength KPR is frequently greater than that from the shorter wavelength WCR, caused by, primarily, two different situations. First, scattering by hydrometeors is similar for both radars as long as particle size constitutes Rayleigh scattering. This includes particles less than about 0.6 mm (<1.5 mm for the KPR but <0.6 mm for the WCR; Fig. 1). When particles exceed 0.6 mm, the power scattered back to the radar no longer increases exponentially with increasing diameter for the WCR. For cases with ice, hydrometeors are generally larger than 0.6 mm, resulting in at least partial Mie scattering at W band, yet in some size range (~0.6–1.5 mm) still Rayleigh scattering at Ka band. Because of this, large particles will increase the DWR magnitude.

Second, the WCR and KPR signals can experience different amounts of absorption. Absorption by gases occurs primarily from water vapor and oxygen (Rauber and Nesbitt 2018, chapter 9.2). Water vapor and oxygen absorption both increase rapidly near 95 GHz (W band), and absorption is significantly less at Ka band. Absorption is generally small over short distances for the atmospheric conditions in this study, about 0.7 dB km^{-1} for W band and 0.1 dB km^{-1} for Ka band (Ulaby et al. 1981, chapter 5.4). Absorption can also occur from the hydrometeors themselves. While KPR experiences minimal absorption due to hydrometeors, except in extreme precipitation events, the WCR signal is susceptible to absorption from liquid drops. This can be useful for estimating the distribution of liquid water content in liquid-only clouds but reduces the DWR and introduces error during the retrieval of ice properties. To correct for liquid attenuation, the average profile of liquid water during the IOP is estimated from a combination of flight-level data and the nearest passive microwave radiometer deployed in SNOWIE (located near the upwind edge of the flight track). The five-channel radiometer data were quality controlled as described in Tessendorf et al. (2020). The vertical distribution of liquid water (Fig. 2) is from a neural network trained by sounding data, and is more uncertain than the integrated path (Weeks 2017); this explains why the profiles are similar on different days. This liquid water profile is used to determine W-band absorption using coefficients in Eq. (12) in Liebe et al. (1989), which has been shown to agree well with observations (Vali and Haimov 2001). Since this study emphasizes close-range DWR estimates (<200 m from the aircraft), the attenuation correction shown in Fig. 2, and their uncertainties, are minimal. When DWR is used at greater range (section 3e), larger uncertainty exists and local enhancements (or reductions) in liquid water cause deviations from the radiometer measured liquid water.

b. *Beam matching*

Both WCR and KPR have the same airborne vantage point of a vertically profiling radar, their footprints overlap and have the same geometry. For the cases considered in this paper, both radars utilize the same range resolution and the same range sampling. Unfortunately, the two radars have significant differences in both beamwidth and along-track resolution. The narrower WCR beam (~0.7°) samples substantially less volume than the KPR beam (~4.2°), especially at large range. The effects of this are further complicated by the

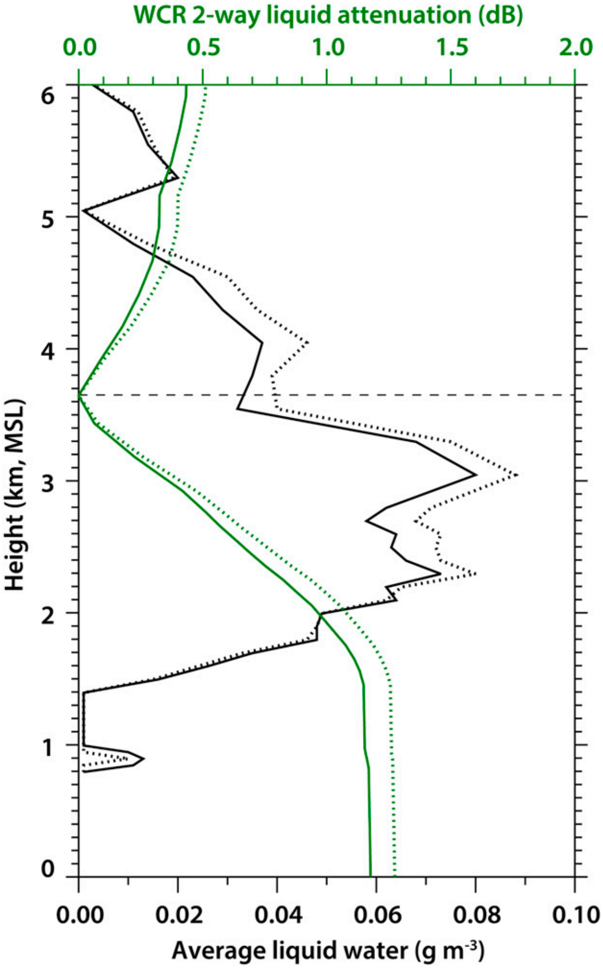

FIG. 2. Radiometer average liquid water profile (black) from the hour preceding IOP 14 (solid) and IOP 16 (dotted) when conditions are similar to the observations by the UWKA. The two-way liquid attenuation applied to the WCR reflectivity is in green and flight level is marked by the dashed horizontal line.

different dwell times of the WCR and KPR (0.045 and 0.20 s, respectively). While reflectivity is an inherent property of particles and normalized by a radar's contributing volume, the presence of additional scatterers within the KPR contributing volume adds uncertainty when comparing the two reflectivity values.

For the most part, this can be corrected for in the *along-track dimension* by Gaussian-weighted averaging of the WCR reflectivity down to the KPR resolution. Gaussian averaging weights the center WCR profiles more in order to match the Gaussian shaped KPR volume. This is accomplished by centered averaging of WCR reflectivity, in linear units, surrounding the center of each KPR profile. The weights depend on the number of WCR profiles that fall within the KPR beam diameter at each range gate and a Gaussian kernel with a standard deviation of one. The beam mismatch in the *cross-track dimension* cannot be corrected for. Assuming optimal averaging is performed in the along-track dimension, the quality of the beam match is limited by the fraction of KPR power that is returned from within the WCR contributing volume, assuming a uniform field of distributed targets. For a Gaussian shaped main lobe pattern, this value is approximately 22%.

At the range used in the following analysis, the KPR beam diameter is about 10 m. The amount of nonuniform beam filling at this scale, and scatterers that differ substantially from what the WCR observed, is likely to be small.

c. *In situ microphysics observations*

A unique strength of the UWKA configuration is the proximity of in situ particle sizing and imaging probes to the DWR values above and below the aircraft. This advantage is used to examine the DWR relationship with snow/ice properties without having to determine adequate proximity in both space and time when the radars and microphysics instruments are on different platforms. Thus, by using SNOWIE data, the only requirement for matching microphysics observations with the radar DWR measurements is to interpolate radar reflectivity across the blind zone near the aircraft by averaging the second gate above and below flight level (i.e., linearly interpolating). The second gate is used because of transmitter leakage affecting the first gate (Fig. 3). The center of this gate is at a range of 120 m for the WCR and 136 m for the KPR, above and below the aircraft. First, we determine "flight-level" reflectivity by linear interpolation between the two range gates, thereby assuming reflectivity varies linearly across flight level. Second, "flight-level" DWR is the difference between KPR and WCR flight-level reflectivity estimates. The flight-level DWR can then be compared to in situ optical array probes (OAP) and IWC probes. Because the radar observations occur a significant distance above and below the in situ particle measurements, some uncertainty is introduced due to vertically nonlinear changes related to wind and ice particles within the radar blind zone.

The Nevzorov hotwire (Korolev et al. 1998) and heated cone (Korolev et al. 2013) are used for estimating liquid water content (LWC) and total water content (TWC). IWC is the difference between the two measurements (TWC − LWC). Both TWC and LWC were manually corrected using observations of liquid and ice from other instruments (French and Behringer 2021). Primarily, this removed liquid bias caused by ice colliding with the hotwire LWC probe. Other uncertainties like the underestimation of TWC due to ice shattering or flowing around the probe remain uncorrected.

Two OAPs are combined to characterize the PSD for diameters between 100 and 1600 μm (French and Majewski 2017). The 2D-Stereo Probe (2DS; Lawson et al. 2006) counts particles from about 10 to 1280 μm with 10 μm bin resolution while the legacy 2D Precipitation Probe (2DP) counts particles from about 400 to 1600 μm with 200 μm bin resolution. The University of Illinois OAP Processing Software (Jackson and McFarquhar 2014; Finlon et al. 2016) removes image artifacts and applies dimensional corrections before the PSDs from the two probes are combined at 1200 μm. By using particle sizes greater than 100 μm, contamination from liquid

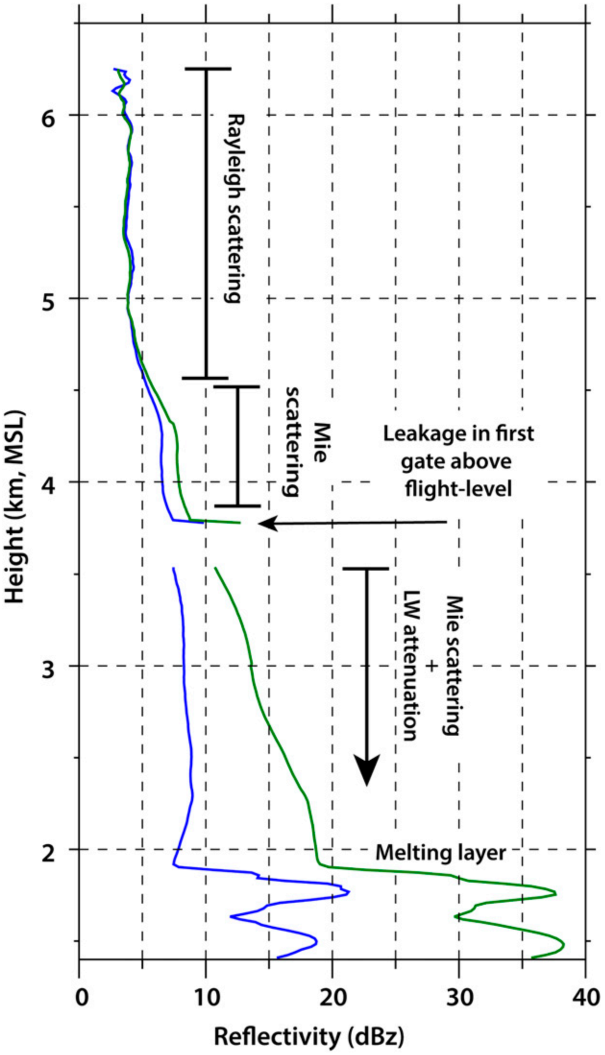

FIG. 3. Average profiles of WCR (blue) and KPR (green) reflectivity from the IOP 14 cross section discussed below.

drops is reduced and the resulting total number concentration ($N_{T,100}$) is close to the ice number concentration. Although the PSD has a time resolution of 1 s, a moving average of 20 s is applied to allow for a sufficient number of the larger particles to be included in the distribution. Other averaging techniques were tested, such as using different moving average lengths and increasing bin widths. There were no significant differences from the 20 s average, which had a good balance between detail and low noise. The same 20 s moving average is applied to the flight-level estimate of reflectivity when it is compared to PSD data.

The median-volume diameter (D_0) is used as the representative particle size for a distribution, which is defined as the nearest particle diameter in the PSD that separates the total solid sphere volume in half. For any particle, its 2DS or 2DP reported diameter is the *maximum* particle dimension. Clearly the assumption of a sphere of that diameter may vastly overestimate the actual ice particle volume, especially for pristine ice crystals. Similar to reflectivity, which is proportional to particle diameter to the sixth power in the Rayleigh regime, the volume diameter is weighted by the largest particles, but only to the third power. Additionally, D_0 is proportional to a mass-weighted diameter without the added assumption of an effective density.

d. *Methodology for Mie–Lorenz calculations*

The equivalent reflectivity factor retrieved from each radar is primarily a function of the particle size distribution $N(D)$ and the backscattering cross section $\sigma(D, \lambda)$ and can be written as

$$Z_e = \frac{\lambda^4}{\pi^5 |K_w|^2} \int_0^\infty N(D)\sigma(D,\lambda)\,dD, \tag{1}$$

where λ is the wavelength and K_w is related to the complex refractive index for water and is a function of the radar frequency and temperature. To estimate $N(D)$, $\sigma(D, \lambda)$ is calculated by assuming that ice particles are homogeneous spheres with some snow density (ρ_s) that is less than the density of pure ice ($\rho_i = 0.9168$ g cm^{-3}). First, the complex permittivity of pure ice (ε_i) is estimated using Hufford (1991) considering the radar frequency and average flight-level temperature. Next, the permittivity of a snow particle (mixture of ice and air) is calculated as described by Meneghini and Liao (2000) where

$$\varepsilon_s = \frac{\rho_i + 2K_i\rho_s}{\rho_i - K_i\rho_s}, \tag{2}$$

$$K_i = \frac{\varepsilon_i - 1}{\varepsilon_i + 2}. \tag{3}$$

Last, the resulting refractive index of the snow particle ($\mathrm{Ri}_s = \sqrt{\varepsilon_s}$), radar wavelength, and particle radii are used to determine the radar cross section of each particle by the process developed by Bohren and Huffman (1983). The results of a snow particle with a density ρ_s of 0.1 g cm^{-3} and $0.1 < D_0 < 10$ mm is shown in Fig. 1. The lower density of an ice particle reduces the reflectivity factor when compared to the Rayleigh assumption. The Mie oscillations of radar reflectivity (Fig. 1a) match what has been calculated by others using different methods (e.g., Fig. 3 in Wang et al. 2005).

e. *WCR and KPR calibration*

The DWR uncertainty is dependent on the relative calibrations of the WCR and KPR while the scattering calculations and other single reflectivity comparisons are dependent on their absolute calibrations. The WCR reflectivity is calibrated by measuring the return from a trihedral corner reflector with a known scattering cross section. Error associated with this calibration is estimated to be less than 2.5 dB (Wendisch and Brenquier 2013, 509–517). KPR calibration was completed off the aircraft by using a signal with known power and fine-tuned by cross calibrating with WCR in regions of drizzle drops smaller than 400 μm (Tripp et al. 2017; Haimov et al. 2018). Due to the cross calibration, the relative calibration

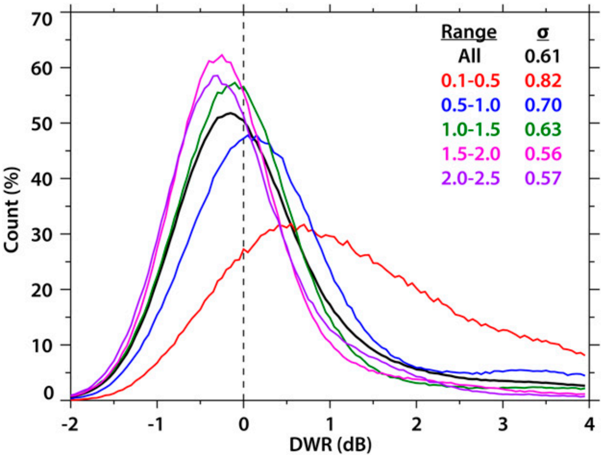

FIG. 4. Histograms of DWR for regions with $0 < Z_{\mathrm{Ka}} < 8\,\mathrm{dB}Z$ expected to be dominated by Rayleigh scattering. The black line includes about 3.5 million points, which are also separated into histograms by range from flight level identified by colors in the figure. The distributions' standard deviations (σ) are used to estimate the relative calibration and KPR absolute calibration listed in Table 1.

between the two radars is quite good, estimated here by investigating the difference between the WCR and KPR (i.e., the DWR) where they are expected to be the same (e.g., where scattering is dominated by Rayleigh scattering). Figure 3 shows an example of WCR and KPR profiles averaged during a period of relative homogeneity (between 60 and 80 km in the Fig. 11 cross section discussed later) and provides insight into reflectivity values when Rayleigh scattering is dominant. The region of expected Rayleigh scattering occurs above 4.5 km where the KPR profile (green) is a close match to the WCR profile (blue). Their difference shrinks rapidly between 5 and 8 dBZ at Ka band. Mie scattering is responsible for the mismatch between 2 and 4.5 km MSL and is the region where retrieving bulk microphysical properties is possible. In Fig. 4, we look at near-cloud-top echoes throughout IOP 14 where KPR reflectivity is between 0 and 8 dB. In these regions of low reflectivity and small ice particles, the DWR is close to 0 dB but has a near-Gaussian spread expected from random error. The standard deviation shows a slight dependence with range; the standard deviation of the DWR within 0.5 km from the aircraft is about 0.8 dB while the distribution narrows at greater range ($\sigma \approx 0.6$ dB between 2 and 2.5 km), likely improved by the additional averaging. Because of the difficulty in separating random error from systematic error in the WCR calibration, values mentioned here and summarized in Table 1 are a total error, assumed to be random in our calculations. The right side of the distributions (with increasing DWR) have additional bias from increasing Mie scattering, preventing a symmetrical curve; thus, symmetry with the left side of the distribution is assumed when calculating standard deviation. Last, the WCR and DWR uncertainties are used to estimate the absolute calibration of the KPR.

3. Comparisons between the DWR and ice median-volume diameter

a. *DWR versus median volume diameter*

For a population of monodisperse ice particles, the expected radar reflectivity is not monotonic, resulting in multiple possible size solutions for a given DWR (Fig. 1b). A natural cloud parcel typically contains a distribution of ice particle sizes. This distribution of particle sizes reduces the oscillatory nature of scattering within the Mie regime so that the radar reflectivity, relative to a particle size representative of the distribution, can be considered monotonic (Fig. 1, solid lines). Given the relationships between D_0 of a population of droplets and radar reflectivity for both W band and Ka band shown in Fig. 1a, the expectation is for the DWR (Ka–W) to increase as the distribution's D_0 increases (Fig. 1b). Furthermore, given sufficiently accurate Mie calculations, it should be possible to relate a measured DWR directly to an expected D_0 between 0.3 and 15 mm (with the assumptions about snow density and shape of the PSD). However, due to the complexities with estimating backscattering cross sections from ice crystal shapes/orientations, we forgo this approach in exchange for comparing the flight-level D_0 directly with the measured flight-level DWR.

Comparison between observed flight-level D_0 and DWR reveals a near exponential relationship for DWR values below ~7.5 dB (Fig. 5). Each 1-s average value of DWR is placed in a bin between 0.0 and 9.5 with bin width of 0.5 dB.

TABLE 1. Summary of the sources of uncertainty and their effects on DWR, D_0, $N_{T,100}$, and IWC valid where DWR is less than 7.5 dB, in ice-dominated clouds such as IOP 14 (LWC < 0.1 g m^{-3}). Italicized values in the last three rows are determined by perturbing DWR and the model by their respective uncertainties in the algorithm.

Uncertainty source	Uncertainty at flight level	Uncertainty away from flight level
WCR calibration (dB)	~2.5	~2.5
KPR calibration (dB)	~3.3	~3.3
Relative calibration (includes 22% beam match) (dB)	~0.8	~0.6
Path-integrated water (liquid) attenuation (dB)	Minimal	<1.0(case dependent)
Scattering model uncertainty (dB)	~3	~3
Total DWR uncertainty (dB)	~0.8	~2.3
Total D_0 uncertainty (mm)	~0.5	*<2*
Total $N_{T,100}$ uncertainty (cm^{-3})	~0.004	*<0.012*
Total IWC uncertainty (g m^{-3})	~0.05	*<0.25*

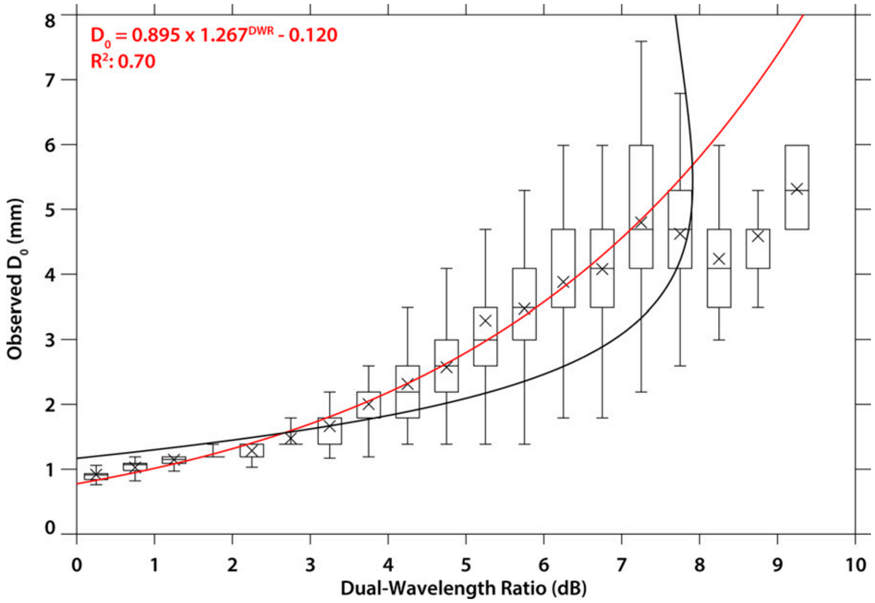

FIG. 5. Flight-level distribution of median volume diameter (D_0) for a range of binned DWR values. Mean values (× symbols) have been fitted with an exponential distribution (red line) excluding the last four bins. Boxplots indicate the range of the data (excluding outliers) and the boxed interquartile range. The black line is the theoretical relation from the scattering model after bias (identified in section 3c) is removed.

To be included in the model, flight-level values from IOP 14 (18 February 2017) must have a KPR reflectivity greater than 0 dBZ, which is above the minimum detectible signal at this range (prior to this, KPR data are filtered to exclude points within three standard deviations of the noise). Additionally, the difference between the radar gate above and below flight level must not exceed 5 dB. These requirements ensure that the measured reflectivity is above the noise and that the precipitation structure is rather uniform across flight level.

The center of each DWR bin is fitted to the average D_0 (× within each boxplot) by least squares assuming an exponential relationship (Fig. 5). The last four bins are not included in this fit; large ice particles encountered are difficult to size by the 2DP because a majority of the particle's cross section likely falls outside the 6.4 mm diode array. The resulting exponential function has the form $D_0(\mathrm{DWR}) = C_1 C_2^{\mathrm{DWR}} + C_3$, where the coefficients $[C_1, C_2, C_3] = [0.895, 1.267, -0.120]$, DWR is in decibels, and D_0 is in millimeters. Compared to theoretical calculations (black line in Fig. 5), the observed DWR (red line in Fig. 5) changes over a larger range of D_0. The Mie theory calculations predict the largest DWR sensitivity for small D_0, especially sizes less than 2 mm. Observations show that the DWR increases in this region, but not as quickly. Both the modeled and observed DWR stop increasing with increasing D_0 between 7 and 8 dB and between 4 and 5 mm. Discrepancy is likely, in part, caused by the limitations of the Mie theory in predicting the backscattering cross sections of ice but may also be caused by changes to the shape of the distribution (examined in the next section) that occur in tandem with changes in D_0. The modeled DWR in Fig. 5 assumes a constant distribution shape while the actual distribution shape likely changes as the number of larger particles increases (explored in the next section). This DWR–D_0 relationship is similar to those in Duffy et al. (2021), although theirs is based on mass-weighted mean diameter.

b. *Estimating the PSD from DWR and reflectivity*

Hydrometeor size distributions can be described using a gamma distribution (e.g., Fig. 6a), which is directly related to the hydrometeor number density (N_0), the snow diameter (D), the median volume diameter (D_0), and the shape parameter (μ) in this modified form described by (Liao et al. 2005):

$$N(D) = N_0 D^{\mu} \exp\left[-(3.67 + \mu)\frac{D}{D_0}\right], \tag{4}$$

$$N_0 = \frac{N_T G^{\mu+1}}{\Gamma(\mu + 1)}, \tag{5}$$

$$G = \frac{3.67 + \mu}{D_0}. \tag{6}$$

Because of the direct relationship between Z_e, $N(D)$, and N_0, and the definition of the dual-wavelength ratio [$\mathrm{DWR} = 10\log(Z_u/Z_v)$], the DWR is independent of ice number concentration and N_0 (Liao et al. 2005). However, there remains some dependence on μ and snow density (ρ_s), in addition to D_0, due to the dependence of the dielectric constant on density (Liao and Meneghini 2000). In Eq. (5), N_T (the total number concentration) is replaced with $N_{T,100}$ ($N_{T,100} = N_T > 100$ μm; units: m^{-3}) and $\Gamma(x)$ indicates the gamma function of x.

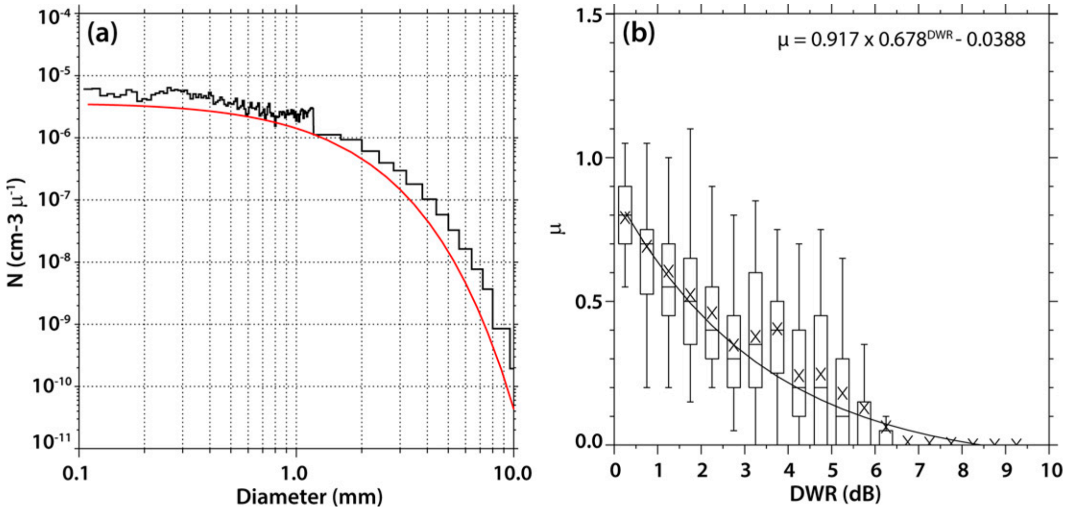

FIG. 6. (a) Observed size distribution (black) and fitted gamma distribution (red) for an example DWR of 5.5 corresponding to a D_0 of 3.2 and the shape parameter μ from the relationship shown in (b) the distribution of best-fit μ for the observed range of DWR values at flight level. The solid black line is an exponential fit to the mean values (× symbols) in each bin.

The gamma shape parameter μ is the greatest contributor to uncertainty when estimating the number concentration from the Mie scattering model. After testing various measured size distributions from IOP 14, each representing 20 s of 2DP data, it appears that $\mu = 0$ is well-suited for representing observed size distributions when the KPR reflectivity and DWR are large (DWR > 3.5), signifying many large particles (Fig. 6a). A shape parameter of 0 reduces the modified gamma distribution to an exponential distribution. Other studies have also found $\mu = 0$ to work well (e.g., Tridon et al. 2019). For smaller KPR reflectivities (and smaller values of DWR), where there are fewer large particles, we found that a larger shape parameter μ is needed to fit the observed PSD. Using all flight level data from IOP 14, each PSD was matched with the best μ using the Kolmogorov–Smirnov method; i.e., minimizing the difference between the two cumulative distribution functions. As expected, the results show that a larger μ fits a PSD better for smaller DWR values (Fig. 6b) and that, overall, small μ values match best for the flight-level observations for this case. The mean μ of each bin in Fig. 6b fits an exponentially decreasing function of the form $\mu(\mathrm{DWR}) = C_4 C_5^{\mathrm{DWR}} + C_6$, where the coefficients $[C_4, C_5, C_6] = [0.917, 0.678, -0.0388]$. Applying this function allows both D_0 and μ to vary as a function of DWR. This function could vary for different cases and cloud dynamics, for example, when there are fewer large hydrometeors and the distribution is more gamma-like with larger values of μ.

c. *Estimating ice number concentration $N_{T,100}$ and particle density ρ_s*

Provided a measurement of DWR (centered at flight level, or elsewhere), the equivalent size distribution can be created by first estimating the D_0 from the flight-level relationship derived in section 3a, and then using Eqs. (4)–(6), with a DWR-dependent shape parameter μ. The values of N_0 and $N_{T,100}$ can be determined by forward modeling of the backscattering cross section within the three-dimensional space of D_0, $N_{T,100}$, and ρ_s (see section 2d) by matching observed and calculated WCR and KPR reflectivity. Single-particle snow density ρ_s is defined as the mass of the particle divided by the volume that envelopes it (Heymsfield et al. 2004)—a sphere with an effective diameter (w.r.t. its scattering properties) in the case of the model. Accurately estimating these ice characteristics relies on the ability of the model to match the observed reflectivity when given the true distribution. To test this, the model is used with a gamma distribution derived from the D_0 observed at flight level. The calculated reflectivity is then compared to the measured "flight-level" reflectivity for both Ka band and W band (Fig. 7). For a perfect scattering model, the calculated and observed reflectivity should be close, within the uncertainties discussed in section 2e; however, error from assuming ice particles are homogeneous and spherical causes a bias that is seen in Fig. 7b.

For IOP 14, there is a mean bias of 7.5 dB between the WCR and KPR reflectivity values: when the ρ_s is adjusted so that the WCR calculated reflectivity matches the observed (the optimal model density is close to 0.1 g cm^{-3} for IOP 14), then the KPR is typically off by 7.5 dB (Fig. 7), confirming the limitations of the Mie model. Raising (lowering) ρ_s increases (decreases) the calculated reflectivity so that it is possible to find the optimal density for one radar while an offset may remain for the other. Because ice particles or aggregates can rarely be classified as homogeneous spheres, the calculated snow density is unlikely to match observed value. The observed value, the *minimum bulk snow density* $\rho_{s,\min}$ is determined by dividing the Nevzorov probe estimated IWC by the total solid sphere volume (Heymsfield et al. 2004). It is expected to be a minimum because particles are characterized by their maximum diameter. Conversely, the snow density within the scattering model (ρ_s) is larger because the effective diameter is smaller than the maximum diameter reported by the OAPs.

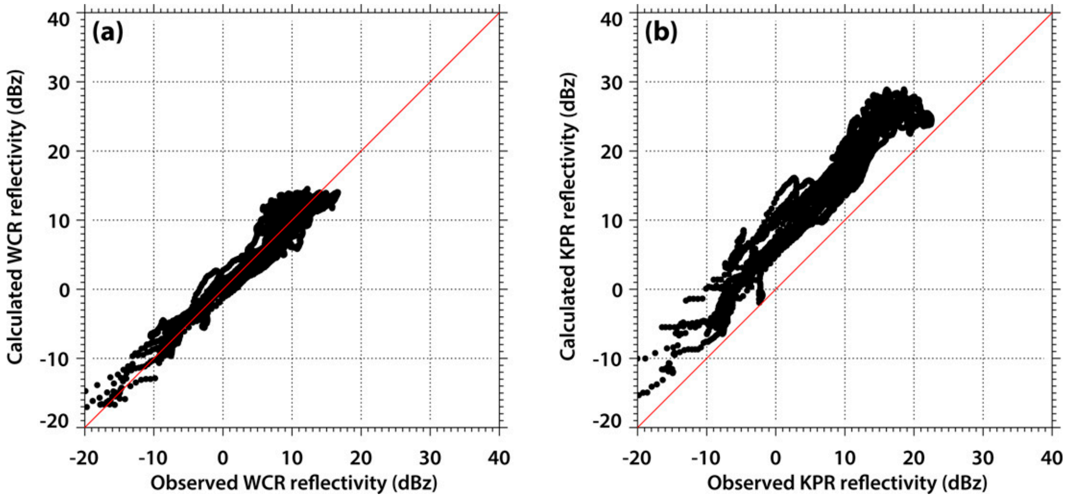

FIG. 7. Comparison between flight-level-centered radar reflectivity and the Mie calculated reflectivity using the observed size distribution for the (a) WCR and (b) KPR. Ice particles are assumed to have a density of 0.1 g cm^{-3}.

Following this discussion, the bias is always removed from the KPR calculated reflectivity. This subtraction shifts the calculated KPR reflectivity down to the red line in Fig. 7b and also reduces the modeled DWR (e.g., Fig. 1b). As a result, it seems that very small D_0 may have a negative DWRs in the model; however, such small D_0 are not observed (partially because small particles contribute very little to D_0, and partially because particles less than 0.1 mm are not included in the distributions). About 0.8 dB of this 7.5 dB bias may be attributed to uncertainty in radar cross calibration (Table 1), but the difference is otherwise attributed to limitations in the Mie calculations. Some of this may arise from the observations where the particle counts and diameters measured by the OAPs differ from what the radar would observe, due to the small sampling volume of the OAP and ice crystal orientations. The smaller OAP sampling volume (compared to the radars) results in an underestimate, while the use of the reported maximum diameter results in an overestimate of the OAP-calculated reflectivity. Once the bias is removed, the expected DWR from the model is typically within the range of observations (black line in Fig. 5).

When this methodology is applied, the Mie model is used with the size distribution (defined by the DWR estimated D_0, and μ in Figs. 5 and 6), to model WCR and KPR reflectivity in the space of ρ_s and $N_{T,100}$. The chosen solution is the ρ_s and $N_{T,100}$ pair that produces the minimum reflectivity difference for both radar wavelengths.

The resulting $N_{T,100}$ values are compared with the flight-level observations in Figs. 8a and 8b. These figures show that a majority of the error in $N_{T,100}$ occurs when the DWR is below about 2.5 dB. For DWR values below 2.5 dB (and the associated D_0 of 1.50 mm) the PSD quickly deviates from an exponential distribution and is only partially compensated for by the shape parameter's dependence on DWR in Fig. 6b. To match the observed reflectivity, the algorithm compensates for the poor match by erroneously increasing (or decreasing) $N_{T,100}$, which is especially noticeable for DWRs below 2.5 dB. The results from this analysis are that $N_{T,100}$ and IWC (and ρ_s) cannot be reliably retrieved when DWR is less than about 2.8 dB (gray points in Fig. 8b). Although this still allows error up to 100%, a majority of points with DWR < 2.8 dB have errors less than 46% for $N_{T,100}$.

The effective snow density that results from the calculation of $N_{T,100}$ does not match with observed $\rho_{s,\min}$ (shown in the next section) for reasons already discussed. In fact, the range of density values used in the algorithm (0.1–0.5 g cm^{-3}), while physically possible being less than the density of ice particles, are about an order of magnitude larger than the observed $\rho_{s,\min}$ (0.01–0.04 g cm^{-3}). Although they are larger than what is estimated from observations, these density values produce backscattering cross sections that match those used in other studies (Wang et al. 2005; Liao et al. 2005). As a result, the large density values produce overestimates of IWC.

In an effort to retrieve a better estimate of IWC we explore ice mass–diameter (m–D) relationships that have been developed by observational and modeling studies that have the form $m = aD^b$. IWC amounts are derived from the observed PSDs by integrating over size bins greater than 100 μm and then are compared to the observed Nevzorov IWC in Fig. 9. Lacking a satisfactory choice of an m–D relationship from those in Fig. 9 (Heymsfield et al. 2004; Brown and Francis 1995; Leinonen and Szyrmer 2015), we test a custom power law with coefficients $a = 0.025$ and $b = 2.07$ (solid green line). While this relationship works well with the observed PSD, it tends to underestimate IWC when applied to the DWR-derived PSD (dashed green line). After testing various power laws, it was found that a simple linear m–D relationship actually worked best for the DWR-derived PSD ($a = 5 \times 10^{-5}$ and $b = 1$, orange lines) and resulted in the smallest root-mean-square error (Fig. 8c). For DWRs greater than 2.8 dB, error is less than 60% with a majority of points having errors less than 17% (Fig. 8d).

d. *Microphysical properties inferred from the DWR–Ka reflectivity space*

It is useful to explore how microphysical characteristics vary in DWR–Z space (e.g., Liao and Meneghini 2016; Kneifel

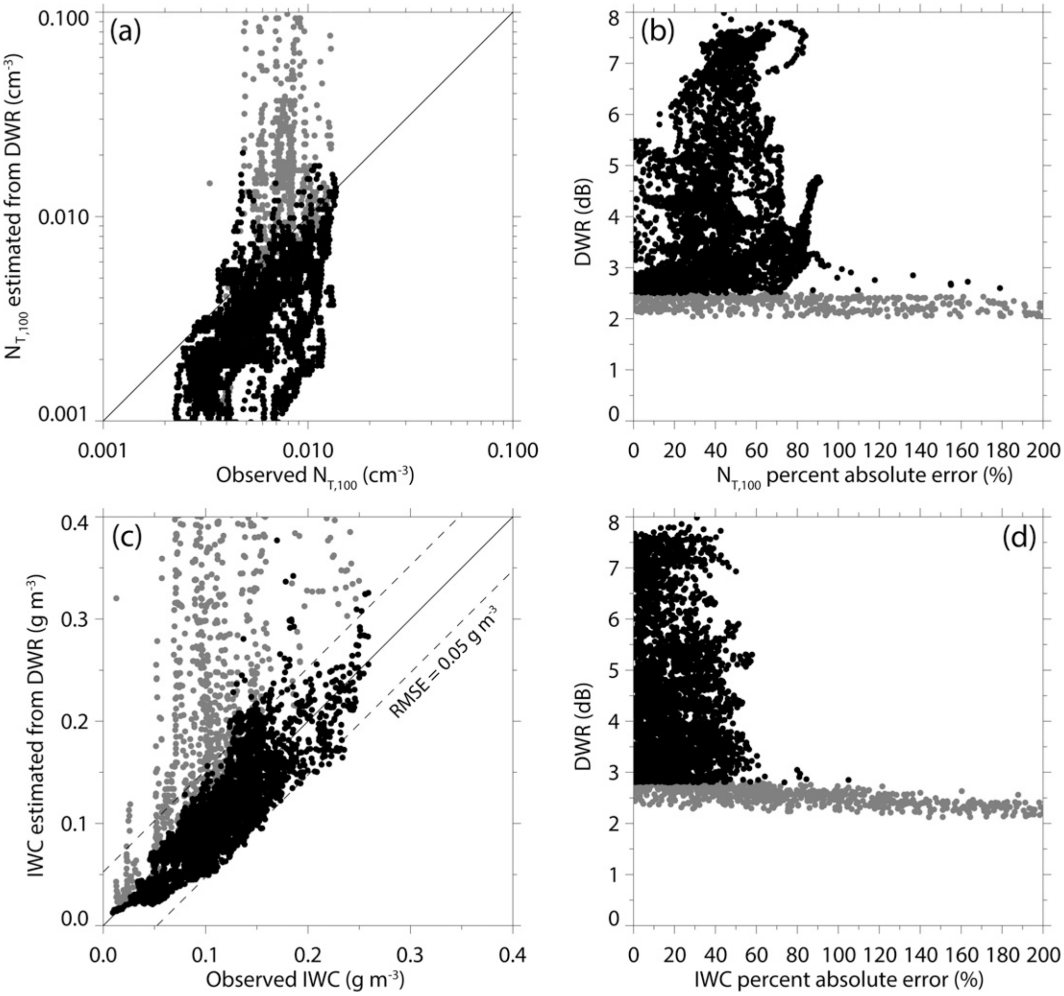

FIG. 8. Observed vs DWR estimated (a) $N_{T,100}$ at flight level and (b) the $N_{T,100}$ percent error vs DWR. (c),(d) As in (a) and (b), but for IWC. Gray dots indicate regions of large error where the DWR is low (<2.8 dB).

et al. 2015; Chase et al. 2018). Here, Z is the reflectivity of one of the two radars (usually the longer wavelength one, KPR in our case), an independent variable. Such an analysis is especially promising here because of the nearly collocated radar and in situ measurements on a single aircraft. Bin-average $\rho_{s,\min}$, D_0, and IWC are plotted in DWR–Z_{Ka} space for the entire flight-level dataset from IOP 14 (Fig. 10). Generally, DWR increases with KPR reflectivity Z_{Ka} and the flight-level DWR maximum is around 9 dB (Fig. 10a), although larger values exist below flight level. Upholding the earlier analysis shown in Fig. 5, D_0 is primarily a function of DWR as shown by most its variation existing in the vertical, along the DWR axis (Fig. 10b). The value of $\rho_{s,\min}$, which is related to ice crystal habit and aggregation, varies along both axes (Fig. 10c). The least dense particles include the largest particles that may include aggregates (large DWR and D_0) but extend to smaller particles with small KPR reflectivity (upper-left regions) and can be associated with more pristine crystals. The highest density is found among the smallest particles for each KPR reflectivity bin (lower-right region). It is expected that these particles experienced little growth, little or no aggregation, and possibly slight riming. Chase et al. (2018) showed a similar inverse behavior between effective density and the Ka–W DWR in their second case. Other studies (Kneifel et al. 2015; Leinonen and Szyrmer 2015) suggest the opposite relationship but focus on riming, of which there is little in IOP 14. Last, IWC appears strongly related to KPR reflectivity. Being a combination of the density and size of particles, small dense particles do not contribute much to IWC and neither do large, low-density particles. The most IWC is found when medium-sized, medium-density particles are present.

e. Algorithm utilization away from flight level (2D cross sections)

The preceding discussions used flight-level comparisons to establish that the DWR is a strong indicator of particle median size D_0. We used this relation to further estimate total

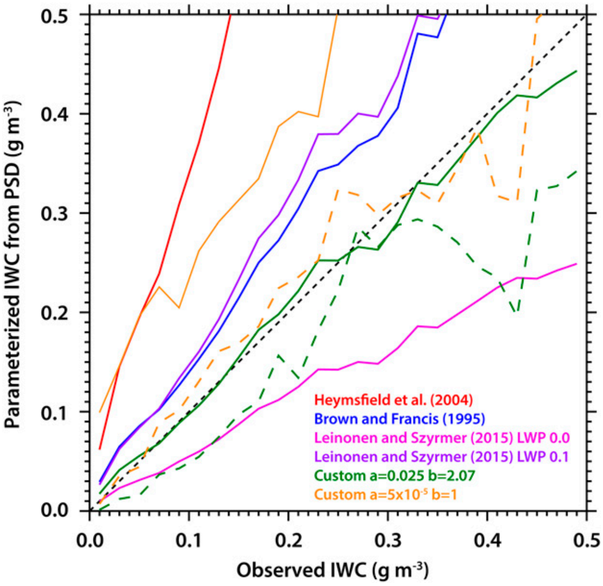

FIG. 9. Observed flight-level IWC compared with IWC derived from published mass–diameter relationships applied to PSDs. The black dashed line is the one-to-one line. Solid green and orange lines use the observed PSD, and dashed green and orange lines indicate the mass–diameter relationship with the DWR-predicted PSD.

number concentration, and IWC, and snow density. These relationships obviously are most useful away from flight level where in situ measurements of cloud microphysics do not exist. Here, we continue using IOP 14 to demonstrate how these derived variables vary away from flight level, with the caveat that retrieved properties have uncertainties, as demonstrated above. An additional caveat is that these relations apply only in ice clouds, with very little cloud liquid water, since the W-band attenuation by droplets is quite high (the two-way path-integrated attenuation is ~10 dBZ km^{-1} g^{-1} m^{-3}) (section 2a), and since the LWC profile is unknown, retrieval uncertainty increases with range to values above those stated in Table 1. Also, imperfect beam matching, which was expected to have a negligible impact on the near-flight-level analysis, has a greater chance of influencing our results at farther range because there is a greater chance of heterogeneity within the larger KPR volume.

In general, our retrieval process is the same as what is described for flight level except for two distinctions. First, no averaging across range gates is performed (unlike flight-level radar products, which are interpolations across the radar blind zone); instead, the only averaging applied is what is described in section 2b for beam matching. This process reduces the DWR resolution with distance from the UWKA. Second, temperature and humidity profiles from a nearby sounding are used to correct for water vapor attenuation following Vali and Haimov (2001). Third, the liquid water profile from a nearby passive microwave radiometer is used to correct for liquid attenuation at W band, following Liebe et al. (1989). Given that the radiometer was on the upstream end of the UWKA transect, the liquid water profile was averaged over the hour preceding the IOP. Assuming that this LWC profile is correct, the maximum path-integrated attenuation is around 1.1 dB at a range corresponding to the subcloud layer just above the ground (Fig. 2). These corrections impact the shorter wavelength WCR reflectivity much more than KPR reflectivity. Given the underlying complex terrain, and the likely occurrence of pockets of higher LWC in the low-level air currents ascending terrain slopes compared to the radiometer site some 50 km upstream (e.g., Rauber and Grant 1987; Xue et al. 2022), the two-way correction can increase the DWR by a few decibels for range gates near the ground, rendering our retrieval less suitable in this environment.

The cross section in Fig. 11 was chosen for the range of DWR values at flight level (0–7 dB) and in the rest of the cross section (up to 10 dB). While there is much variability in KPR (Fig. 11a) and WCR reflectivity (Fig. 11b), the DWR (Fig. 11c) and D_0 (Fig. 11e) generally increases toward the surface as expected from growing/aggregating ice particles. Cross sections and profiles of retrieved variables in Mason et al. (2018) also find that the median diameter of ice increases toward the surface. Because most ice particles fall in the Mie regime at W band, WCR reflectivity is only weakly sensitive to changes in ice particle size. Although the regions between 30 and 60 km and between 70 and 90 km have similar reflectivity values, the DWR reveals that the upstream region (30–60 km) has much larger particles. These large particles are beneath a region of Kelvin–Helmholtz waves analyzed in Grasmick and Geerts (2020) and Grasmick et al. (2021). The reflectivity cross sections also feature a melting layer near 1.7 km MSL where the presence of liquid dictates that the assumptions made in the DWR analysis are no longer valid, so we focus our attention above the melting level and regions below are blackened out. For the range of DWR at flight level, the predicted D_0 closely follows the observed value, deviating slightly where there is large vertical variability across flight level. Some regions of DWR have increased uncertainty and are either marked or removed. First, DWR uncertainty away from flight level may exceed 2 dB (Table 1) so any retrieved variables where DWR is less than 3 dB is removed (e.g., black region near cloud top in Fig. 11d). Additionally, the D_0 expected from large DWR values (DWR > 7.5) go beyond the exponential relationship observed by the in situ probes (Fig. 5). These D_0 values cannot be verified at flight level so are contoured in the cross sections (Figs. 11c,d) to identify the uncertainty.

Additional microphysical insight may be retrieved by the forward modeling of Mie scattering. Ice concentration and IWC are estimated for the cross section where the DWR is greater than 2.8 dB. Ice concentrations vary from 0.001 to 0.1 cm^{-3} (Fig. 12a), which agrees with flight-level data (Fig. 12c). IWC (Fig. 12b) also shows reasonable values, typically below 0.5 g m^{-3} but a few regions close to the ground reach values greater than 2 g m^{-3}. This may be an overestimate, on account of excessive DWR values, due to an underestimation of low-level LWC and insufficient W-band attenuation correction. In fact, the pockets of very high IWC

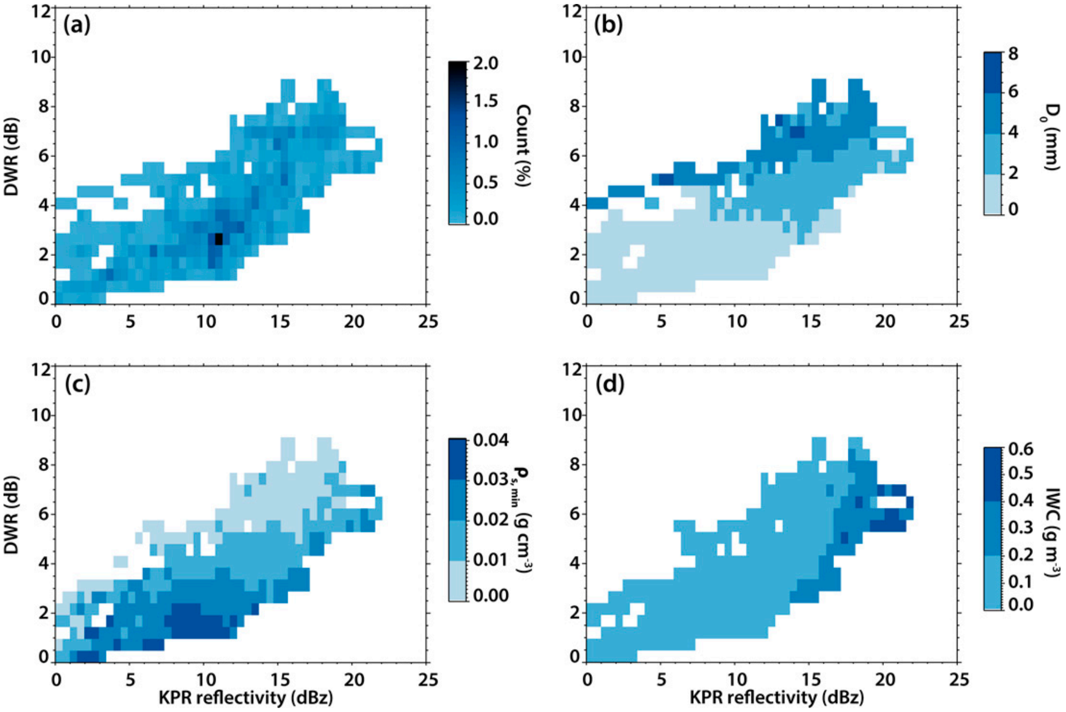

FIG. 10. (a) 2D histogram of point density within DWR–KPR reflectivity space at flight level during IOP 14. Bin average values of (b) D_0, (c) ice particle density, and (d) IWC for the same space, all based on in situ probes.

in Fig. 12b may be markers of pockets of high LWC (located just above). In any event, flight-level observed and modeled IWC are generally in close agreement where DWR $>$ 2.8 (Fig. 8d), even in the contoured regions where D_0 is uncertain. Retrieved IWC has little sensitivity to the shape parameter (Delanoë et al. 2005) but large uncertainty in $N_{T,100}$ and ρ_s for small DWRs drive the error. Within/beneath the KH wave fallstreaks, $N_{T,100}$ is slightly larger and there is a plume of enhanced IWC descending to the surface (although within the contoured region). Also note the retrieved high ice particle concentrations near cloud top in the region with KH billows (marked in Fig. 11).

While an m–D relationship is used in place of snow density to estimate IWC in Fig. 12, the forward modeling of Mie scattering also produces an independent estimate of snow density (see section 2d) within the same transect (Fig. 13a). Compared to the flight-level estimate of $\rho_{s,\min}$, the Mie estimate is more than an order of magnitude too large, as mentioned earlier (Fig. 13b). Even so, the variation in the resulting snow densities appear within expected values; the trends in the estimated density match the trends in the flight-level observations (Fig. 13b). Furthermore, this transect shows that snow density decreases toward the ground as expected from aggregating snow with increasing maximum diameters and more spherical volumes (Heymsfield et al. 2004). Although the density values are too large, the realistic variations in density show that the model is sensitive to changes in snow density and add confidence to our results. In contrast to these results, Mason et al. (2018) typically show density increasing toward the surface. This difference may be caused by our conditions being dominated by aggregation instead of riming. Also, Mason et al. (2018) used a different definition of density in their retrievals (see their density factor).

4. Algorithm testing on separate data (IOP 16)

The results of the DWR algorithm presented in Figs. 7 and 9–12 are based on the combined in situ and radar data the algorithm was developed from. To test the sensitivity of the algorithm to this data, and whether it can be extended to other environmental conditions, we use the same process on a different dataset, IOP 16 (20 February 2017). The conditions during IOP 16 (Fig. 14) were similar to IOP 14 (only 2 days later) but were more unstable/convective, had less homogenous cloud depths, and contained slightly more supercooled liquid (Fig. 2). Like IOP 14, there is an apparent melting layer just below 2 km MSL and there is substantial shear between 5.5 and 7.5 km MSL. The wind speed increases from 27 to 64 m s^{-1} in this layer resulting in a critical Richardson number and Kelvin–Helmholtz instability that can be seen in vertical velocity (not shown). IOP 16 also has larger flight-level DWR values, exceeding 10 dB (Fig. 14c), while the maximum flight-level values in IOP 14 are about 7 dB. The resulting D_0 field suggests that the exponential relationship developed from IOP 14 can be extended to the larger DWR values here; the predicted and observed flight-level D_0 both reach about 7 mm for the largest DWR near $x = 60$ km. Note that there is some disagreement at flight level due to difficulties estimating flight-level

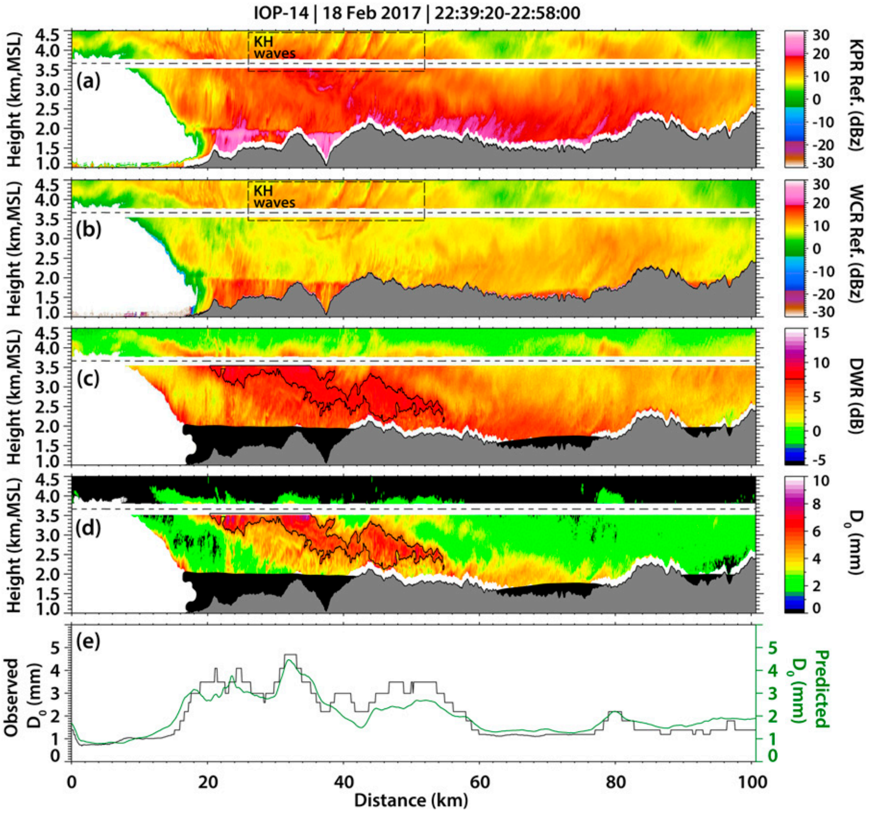

FIG. 11. 2D cross section from IOP 14 over complex terrain, showing (a) KPR reflectivity, (b) WCR reflectivity, (c) KPR–WCR DWR, (d) estimated D_0 using the relationship in Fig. 5, and (e) observed (black) and DWR-estimated (green) flight-level D_0. The dashed line in (a)–(c) is the flight level. The black contour in (c) and (d) indicate where the DWR is greater than 7.5 dB and D_0 is more uncertain. The storm motion is from left to right. Data where DWR is less than 3 dB are covered in (d) as are data below the melting layer.

DWR where large cross flight-level variability exists (e.g., $64 < x < 72$ km). Additionally, near-flight-level shear causes a displacement with in situ observations (seen best in Fig. 15d).

The DWR derived ice concentration and IWC cross sections show unique, small-scale structure within the low-level cloud (Fig. 15). Where convective plumes exist, the ice concentrations near cloud top are large, likely indicative of ice initiation (black boxes in Fig. 15a), and similar to examples in Mason et al. (2018). The temperature at 5 km MSL is about −17°C. These large values are diminished below cloud top as aggregation occurs. Compared at flight level, derived and observed ice concentrations agree quite well, especially when flying in the deepest part of the cloud where the largest DWR exists. The high ice concentrations above the terrain may be the result of ice multiplication processes (the temperature at 2.5 km MSL is about −3°C), although they may be spurious, on account of underestimated LWC. The latter concern applies to the pockets of very high retrieved IWC as well (Fig. 15b). In most of the cloud, the IWC is less than 0.5 g m^{-3}, similar to the previous case. However, within the deepest plume, fall-streaks of high IWC are observed above flight level (around 60 km). These high IWC plumes are confirmed by flight-level observations although slightly displaced from the DWR observation (Fig. 14d).

Similar to the first case, when the variables of interest are averaged within 2D bins, they are sorted into distinctive regions (Figs. 16a–d). Due to increased flight-level liquid water in this case, IOP 16 had locations of instrument icing and, after identifying and removing the affected data, there were fewer good-quality flight-level data segments. Nevertheless, the patterns remain similar to IOP 14. The distribution of D_0 and IWC are nearly identical to what was observed in IOP 14 (Figs. 10b,d): D_0 increases with DWR, and IWC increases with Z_{Ka} (Figs. 16b,d). The distribution of $\rho_{s,\min}$ (Fig. 16c) is not as distinct as other variables or the previous case but still tends to increase toward the bottom right (large Z_{Ka}, small DWR). The range of density values in this case is about twice that in IOP 14. This is probably related to the higher amounts of liquid water and more frequent riming.

5. Discussion

Multifrequency profiling radar reflectivity can be used to characterize cloud and precipitation throughout the depth of

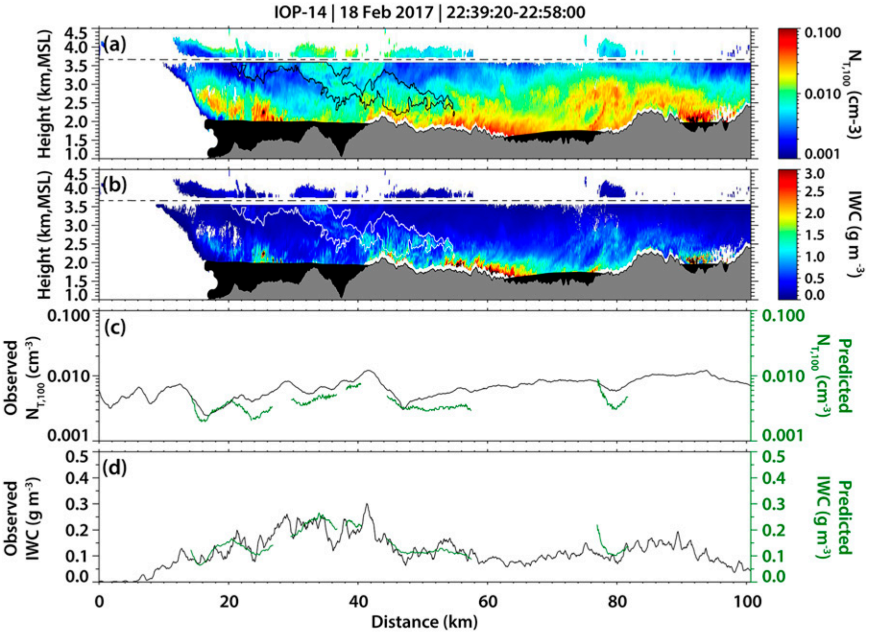

FIG. 12. As in Figs. 11c and 11d, but for the results from the Mie model including (a) ice concentration for particles >0.1 mm and (b) IWC using orange relationship in Fig. 9. (c),(d) Flight-level observed (black) and modeled (green) (c) concentration of ice particles larger than 0.1 mm and (d) IWC. The lack of data near cloud top in (a) and (b) is a result of DWR dropping below 3.0 dB.

a cloud, particularly in mixed-phase clouds. Vertical transects of retrieved microphysical information such as D_0, $N_{T,100}$, and IWC, combined with hydrometeor vertical motion, are essential for understanding mixed-phase precipitation processes. Here, we use two airborne profiling radars, one at W band and one at Ka band, to examine the relationship between DWR and ice particle properties documented with in situ probes. By assuming a shape for the size distribution, a model of ice backscattering cross sections was used to test retrievals of $N_{T,100}$ and, by extension, IWC. In this application, both reflectivity values are used to allow snow density to vary in the scattering model. Instead of using density, a mass–diameter relationship suitable for the small liquid water path conditions is used to estimate the IWC. Like with D_0, estimates of $N_{T,100}$ and IWC match reasonably well with flight-level measurements. Additional information is available via retrieved ice density although there is greater uncertainty because the measurement-derived density and modeled density are not equivalent estimates. The two density estimates behave similarly but differ by about an order of magnitude (Fig. 13b), the observed $\rho_{s,\min}$ being smaller. Even so, using both WCR and KPR to solve for ice density produced much better results than holding ice density constant.

Two cases were presented here for the purpose of demonstrating the development of the DWR algorithm. They provide insight into the usefulness and limitations of such an

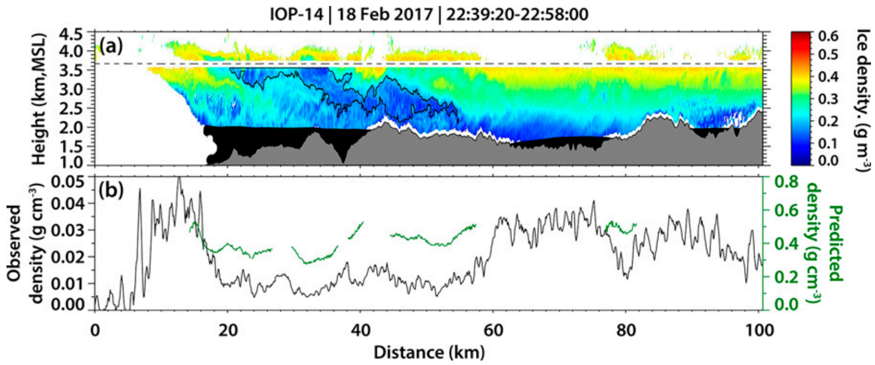

FIG. 13. Ice density output from the Mie model for (a) the cross section presented in Figs. 10 and 11 and (b) retrieved flight-level ice density (green) compared to observed $\rho_{s,\min}$ (black).

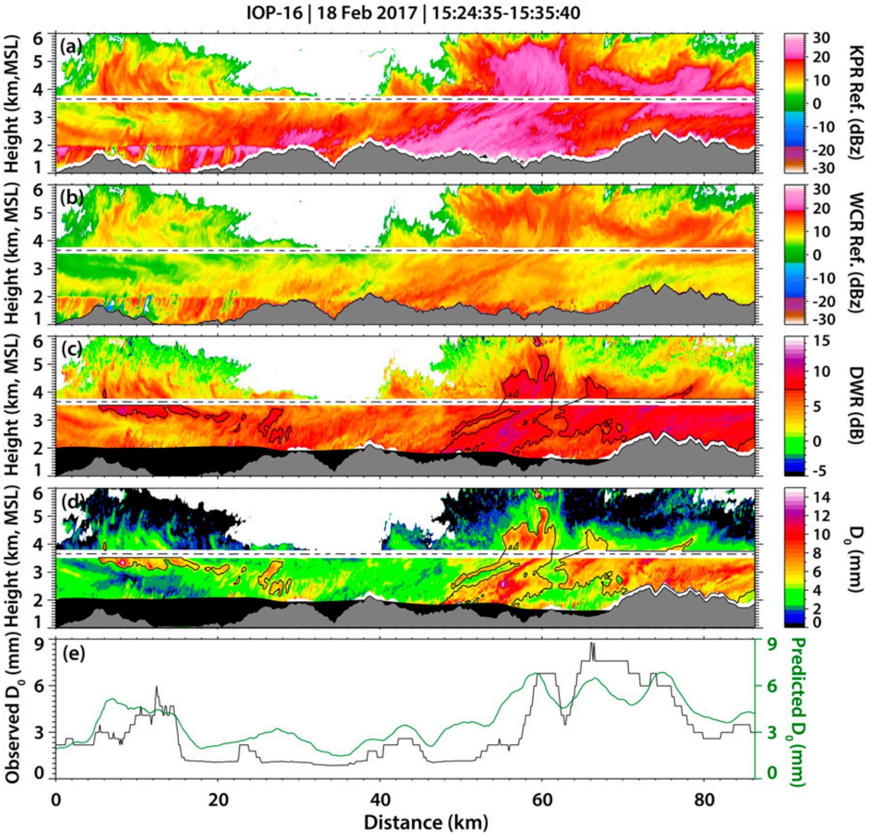

FIG. 14. As in Fig. 11, but for IOP 16.

analysis. In the first case (IOP 14), elevated values of $N_{T,100}$ and IWC in a stratiform cloud can be tracked back to a train of Kelvin–Helmholtz waves known to increase supercooled liquid and riming (e.g., Barnes et al. 2018; Grasmick et al. 2021). In the second case (IOP 16), convective plumes close to cloud top contain dramatic gradients of ice particle concentration likely related to ice nucleation. In both cases, ice particle concentration generally increases toward the surface (Figs. 12a, 15a) in a temperature range between about −10° and 0°C. This may be evidence for secondary ice production, which often occurs in this temperature range in the presence of liquid water (Field et al. 2017).

Flight-level comparisons provide a range of uncertainty when estimating ice particle characteristics using the DWR algorithm. Contributions to this uncertainty come from assumptions made in the retrieval and uncertainty in the measurements (including beam mismatch). D_0 has the smallest uncertainty, which is less than 0.5 mm for a DWR less than ~4 dB but it can increase to around 2 mm for larger DWR (Fig. 5, Table 1). Any uncertainty for DWR larger than 7.5 dB is poorly quantified because of limitations measuring large particles and the rarity with which large DWR values occur at flight level, which in IOP 14 was mostly in the upper cloud region. While a small DWR reduces uncertainty in D_0, it increases uncertainty for variables retrieved with the Mie scattering model, especially $N_{T,100}$ and ρ_s; when particles are small (DWR < 2.5), the backscattering cross sections for the two wavelengths are less sensitive to snow density and there is not a unique ($N_{T,100}$, ρ_s) solution. Excluding these regions, a majority of $N_{T,100}$ estimates have error less than 46% and a majority of IWC estimates have error less than 17% (rmse = 0.05 g m^{-3}, Fig. 8c).

The uncertainty for retrieved variables away from flight level is difficult to fully quantify (Table 1, second column). We estimate it by perturbing the DWR and the scattering model reflectivity by their respective uncertainties. The results, when compared with flight level, give the range of possible errors. This does not quantify the error in the large (>7.5 dB) DWR regions. The uncertainty given in Table 1 is specific to IOP 14. Range-dependent uncertainty is larger in mixed-phase clouds with significant (but unquantifiable) amounts of liquid water. In general, uncertainty away from flight level can be large and additional work is needed to reduce it. Improvements to this DWR retrieval application are achievable, mainly, through improvements to the ice backscattering model but also through additional observations of snow characteristics in large DWR regions, closer to the ground. Alternately, the addition of a third radar wavelength, X band, may help distinguish snow characteristics when the Ka–W DWR saturates.

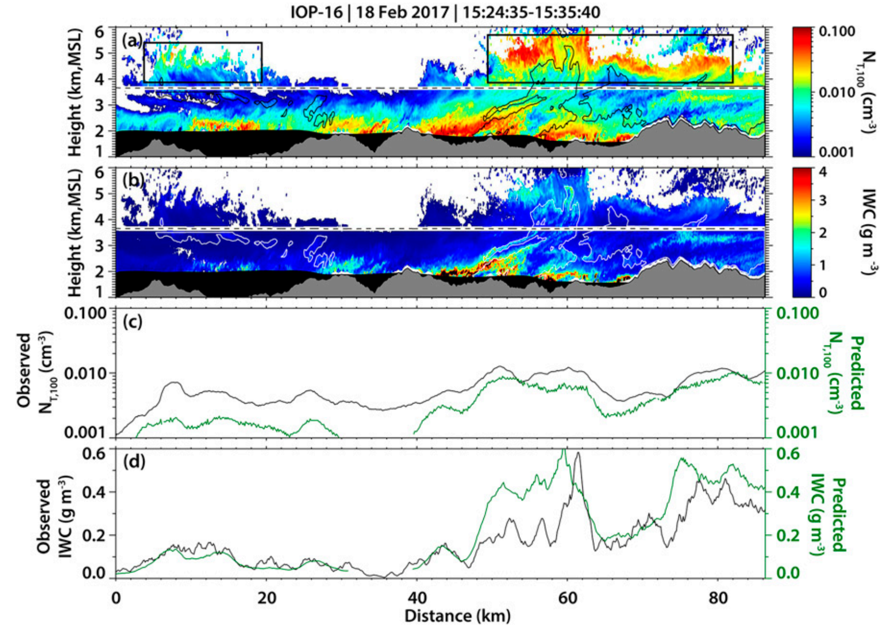

FIG. 15. As in Fig. 12, but for IOP 16. (a) Boxes in mark regions of height number concentrations mentioned in the text.

Coincident in situ and airborne triple-frequency observations during the Radar Snow Experiment show that, for large particles, the X–Ka DWR is more useful for distinguishing D_0 and ρ_s (Nguyen et al. 2022).

More advanced scattering models with fewer limitations and more realistic assumptions in regard to hydrometeor shape have been developed. For example, the snowScatt tool, based on the self-similar Rayleigh–Gans approximation, can estimate the scattering properties of various snowflake aggregates with different monomer compositions and different amounts of riming (Ori et al. 2021). This makes scattering properties of complex shapes and densities more accessible

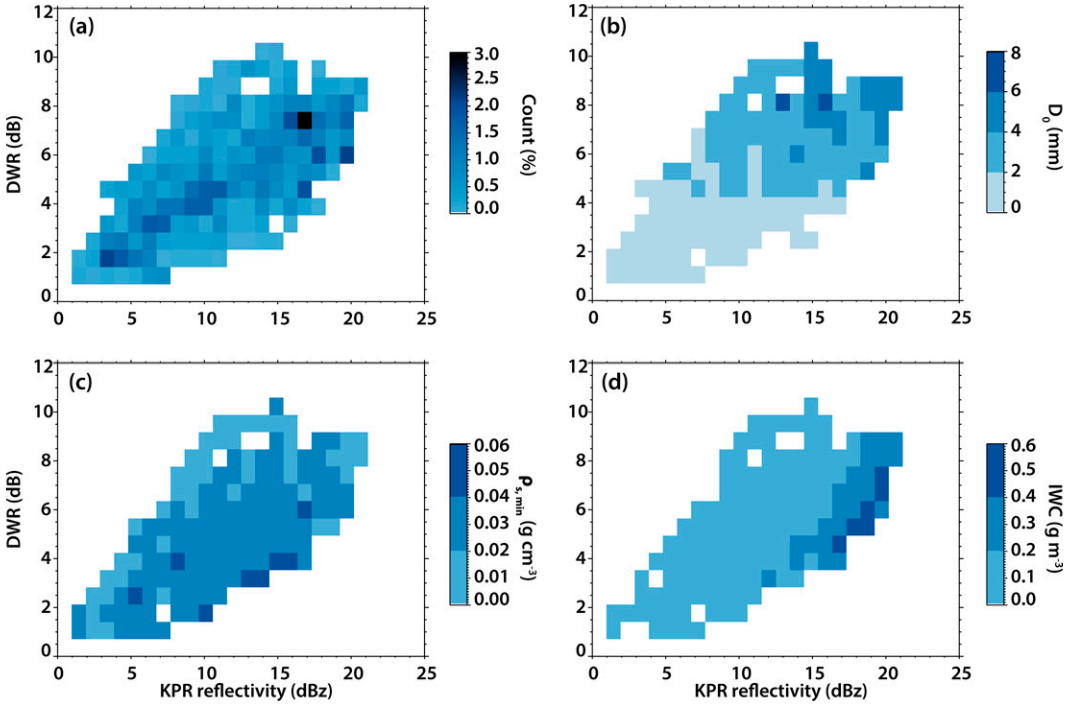

FIG. 16. As in Fig. 10, but for IOP 16.

than previous T-matrix solutions and discrete dipole approximations, which require high computational resources. In this paper, the spherical assumption used in the Mie calculations limits our degrees of freedom, which makes computation simple but can introduce larger errors for aggregates or other crystals with complex shapes that deviate significantly from sphericity.

6. Conclusions

This study uses two airborne profiling radars, one at W band and one at Ka band, in combination with in situ particle sizing probes and a bulk IWC probe, to examine the relationship between the dual-wavelength ratio (DWR) and an ice distributions median-volume diameter. The DWR is also compared with in situ measurements of bulk snow density and IWC. Experimental gamma size distribution and a bulk mass–diameter relations are assumed for the ice particles. These are used with a Mie scattering model to estimate snow density, ice particle number concentration, and IWC from DWR. The main conclusions from the analysis of two flights through ice-dominated clouds are as follows:

- The combination of "flight-level" DWR (an average using radar gates ~140 m below and above flight level) with in situ cloud probes is a powerful tool to refine multifrequency-based precipitation characterization. When placed in the 2D bins, observations of D_0, bulk snow density, $N_{T,100}$, and IWC have consistent, replicable patterns that could be used in future retrieval methods.
- The relationship between D_0 of an ice PSD and the Ka–W DWR appears well-behaved. A larger DWR corresponds to a greater number of large, Mie-scattering particles and a larger D_0 for a PSD. This is useful for identifying locations of large ice particles where processes such as aggregation or rapid deposition or accretion are occurring.
- Forward modeling of backscattering cross sections, in conjunction with the radars' reflectivity and DWR-estimated PSD, can be used to estimate $N_{T,100}$, IWC, and potentially ice density. Model limitations, PSD shape error, and the undocumented presence of LW can cause large uncertainties when retrieving these variables, especially at far ranges. However, the overall success, shown by comparisons with flight-level data, support further algorithm development and the incorporation of more sophisticated scattering models that will reduce the current limitations.

Acknowledgments. We are grateful to Adam Majewski for help with processing OAP data and to Dalton Behringer for the manually corrected Nevzorov IWC. This study was funded by the National Science Foundation Grants AGS-1547101, AGS-1546939, AGS-2016106, and AGS-2016077 and the Wyoming NASA Space Grant Consortium, NASA Grant NNX15AI08H. Funding for the deployment of the University of Wyoming King Air in SNOWIE was funded by AGS-1441831.

Data availability statement. Data collected during the SNOWIE Campaign are available to the public from the Earth Observing Laboratory data archive hosted by the National Center for Atmospheric Research. Flight-level aircraft measurements can be retrieved from https://doi.org/10.15786/M2MW9F (University of Wyoming Research Flight Center 2017a) and WCR data can be retrieved from https://doi.org/10.15786/M2CD4J (University of Wyoming Research Flight Center 2017b). KPR data are available upon request.

REFERENCES

Barnes, H. C., J. P. Zagrodnik, L. A. McMurdie, A. K. Rowe, and R. A. Houze Jr., 2018: Kelvin–Helmholtz waves in precipitating midlatitude cyclones. *J. Atmos. Sci.*, **75**, 2763–2785, https://doi.org/10.1175/JAS-D-17-0365.1.

Bohren, C. F., and D. R. Huffman, 1983: *Absorption and Scattering of Light by Small Particles.* John Wiley and Sons, 530 pp.

Brown, P. R. A., and P. N. Francis, 1995: Improved measurements of the ice water content in cirrus using a total-water probe. *J. Atmos. Oceanic Technol.*, **12**, 410–414, https://doi.org/10.1175/1520-0426(1995)012<0410:IMOTIW>2.0.CO;2.

Chase, R. J., and Coauthors, 2018: Evaluation of triple-frequency radar retrieval of snowfall properties using coincident airborne in situ observations during OLYMPEX. *Geophys. Res. Lett.*, **45**, 5752–5760, https://doi.org/10.1029/2018GL077997.

Delanoë, J., A. Protat, J. Testud, D. Bouniol, A. J. Heymsfield, A. Bansemer, P. R. A. Brown, and R. M. Forbes, 2005: Statistical properties of the normalized ice particle size distribution. *J. Geophys. Res.*, **110**, D10201, https://doi.org/10.1029/2004JD005405.

Duffy, G., G. McFarquhar, S. W. Nesbitt, and R. Bennartz, 2021: Demonstration of a consistent relationship between dual-frequency reflectivity and the mass-weighted mean diameter in measurements of frozen precipitation from GCPEX, OLYMPEX, and MC3E. *J. Atmos. Sci.*, **78**, 2533–2547, https://doi.org/10.1175/JAS-D-20-0174.1.

Field, P. R., 1999: Aircraft observations of ice crystal evolution in an altostratus cloud. *J. Atmos. Sci.*, **56**, 1925–1941, https://doi.org/10.1175/1520-0469(1999)056<1925:AOOICE>2.0.CO;2.

——, and Coauthors, 2017: Secondary ice production: Current state of the science and recommendations for the future. *Ice Formation and Evolution in Clouds and Precipitation: Measurement and Modeling Challenges*, *Meteor. Monogr.*, No. 58, Amer. Meteor. Soc., https://doi.org/10.1175/AMSMONOGRAPHS-D-16-0014.1.

Finlon, J. A., G. M. McFarquhar, R. M. Rauber, D. M. Plummer, B. F. Jewett, D. Leon, and K. R. Knupp, 2016: A comparison of X-band polarization parameters with in situ microphysical measurements in the comma head of two winter cyclones. *J. Appl. Meteor. Climatol.*, **55**, 2549–2574, https://doi.org/10.1175/JAMC-D-16-0059.1.

——, ——, S. W. Nesbitt, R. M. Rauber, H. Morrison, W. Wu, and P. Zhang, 2019: A novel approach for characterizing the variability in mass–dimension relationships: Results from MC3E. *Atmos. Chem. Phys.*, **19**, 3621–3643, https://doi.org/10.5194/acp-19-3621-2019.

French, J. R., and A. Majewksi, 2017: UW King Air hydrometeor size spectra data, version 1.0. UCAR/NCAR Earth Observing Laboratory, accessed 22 December 2017, https://doi.org/10.5065/D6GT5KXK.

——, and D. Behringer, 2021: UW King Air manually corrected Nevzorov liquid/total/ice water content, version 1.0. UCAR/NCAR Earth Observing Laboratory, accessed 10 June 2021, https://doi.org/10.26023/2QRK-XSBA-RS0P.

Grasmick, C., and B. Geerts, 2020: Detailed dual-Doppler structure of Kelvin–Helmholtz waves from an airborne profiling radar over complex terrain. Part I: Dynamic structure. *J. Atmos. Sci.*, **77**, 1761–1782, https://doi.org/10.1175/JAS-D-19-0108.1.

——, ——, X. Chu, J. R. French, and R. M. Rauber, 2021: Detailed dual-Doppler structure of Kelvin–Helmholtz waves from an airborne profiling radar over complex terrain. Part II: Evidence for precipitation enhancement from observations and modeling. *J. Amos. Sci.*, **78**, 3455–3472, https://doi.org/10.1175/JAS-D-20-0392.1.

Grecu, M., L. Tian, G. M. Heymsfield, A. Tokay, W. S. Olson, A. J. Heymsfield, and A. Bansemer, 2018: Nonparametric methodology to estimate precipitating ice from multiple-frequency radar reflectivity observations. *J. Appl. Meteor. Climatol.*, **57**, 2605–2622, https://doi.org/10.1175/JAMC-D-18-0036.1.

Haimov, S., J. R. French, B. Geerts, Z. Wang, A. Rodi, and A. Pazmany, 2018: Compact airborne Ka-band radar: A new addition to the University of Wyoming Aircraft for atmospheric research. *2018 IEEE Int. Geoscience and Remote Sensing Symp.*, Valencia, Spain, IEEE, 897–900, https://doi.org/10.1109/IGARSS.2018.8519605.

Heymsfield, A. J., A. Bansemer, C. Schmitt, C. Twohy, and M. R. Poellot, 2004: Effective ice particle densities derived from aircraft data. *J. Atmos. Sci.*, **61**, 982–1003, https://doi.org/10.1175/1520-0469(2004)061<0982:EIPDDF>2.0.CO;2.

Hogan, R. J., A. J. Illingworth, and H. Sauvageot, 2000: Measuring crystal size in cirrus using 35- and 94-GHz radars. *J. Atmos. Oceanic Technol.*, **17**, 27–37, https://doi.org/10.1175/1520-0426(2000)017<0027:MCSICU>2.0.CO;2.

——, N. Gaussiat, and A. J. Illingworth, 2005: Stratocumulus liquid water content from dual-wavelength radar. *J. Atmos. Oceanic Technol.*, **22**, 1207–1218, https://doi.org/10.1175/JTECH1768.1.

——, L. Tian, P. R. A. Brown, C. D. Westbrook, A. J. Heymsfield, and J. D. Eastment, 2012: Radar scattering from ice aggregates using the horizontally aligned oblate spheroid approximation. *J. Appl. Meteor. Climatol.*, **51**, 655–671, https://doi.org/10.1175/JAMC-D-11-074.1.

Hou, A. Y., and Coauthors, 2014: The Global Precipitation Measurement mission. *Bull. Amer. Meteor. Soc.*, **95**, 701–722, https://doi.org/10.1175/BAMS-D-13-00164.1.

Hufford, G., 1991: A model for the complex permittivity of ice at frequencies below 1 THz. *Int. J. Infrared Millimeter Waves*, **12**, 677–682, https://doi.org/10.1007/BF01008898.

Jackson, R. C., and G. M. McFarquhar, 2014: An assessment of the impact of antishattering tips and artifact removal techniques on bulk cloud ice microphysical and optical properties measured by the 2D cloud probe. *J. Atmos. Oceanic Technol.*, **31**, 2131–2144, https://doi.org/10.1175/JTECH-D-14-00018.1.

Kneifel, S., M. S. Kulie, and R. Bennartz, 2011: A triple-frequency approach to retrieve microphysical snowfall parameters. *J. Geophys. Res.*, **116**, D11203, https://doi.org/10.1029/2010JD015430.

——, A. von Lerber, J. Tiira, D. Moisseev, P. Kollias, and J. Leinonen, 2015: Observed relations between snowfall microphysics and triple-frequency radar measurements. *J. Geophys. Res. Atmos.*, **120**, 6034–6055, https://doi.org/10.1002/2015JD023156.

Korolev, A. V., J. W. Strapp, G. A. Isaac, and A. N. Nevzorov, 1998: The Nevzorov airborne hot-wire LWC–TWC probe: Principle of operation and performance characteristics. *J. Atmos. Oceanic Technol.*, **15**, 1495–1510, https://doi.org/10.1175/1520-0426(1998)015<1495:TNAHWL>2.0.CO;2.

——, ——, ——, and E. Emery, 2013: Improved airborne hot-wire measurements of ice water content in clouds. *J. Atmos. Oceanic Technol.*, **30**, 2121–2131, https://doi.org/10.1175/JTECH-D-13-00007.1.

Kumjian, M. R., 2013: Principles and applications of dual-polarization weather radar. Part II: Warm- and cold-season applications. *J. Oper. Meteor.*, **1**, 243–264, https://doi.org/10.15191/nwajom.2013.0120.

Lawson, R. P., D. O'Connor, P. Zmarzly, K. Weaver, B. Baker, Q. Mo, and H. Jonsson, 2006: The 2D-S (stereo) probe: Design and preliminary tests of a new airborne, high-speed, high-resolution particle imaging probe. *J. Atmos. Oceanic Technol.*, **23**, 1462–1477, https://doi.org/10.1175/JTECH1927.1.

Leinonen, J., and W. Szyrmer, 2015: Radar signatures of snowflake riming: A modeling study. *Earth Space Sci.*, **2**, 346–358, https://doi.org/10.1002/2015EA000102.

——, D. Moisseev, and T. Nousiainen, 2013: Linking snowflake microstructure to multi-frequency radar observations. *J. Geophys. Res. Atmos.*, **118**, 3259–3270, https://doi.org/10.1002/jgrd.50163.

Liao, L., and R. Meneghini, 2000: Investigation of the dielectric constants of inhomogeneous air-ice and snow-water spheres. *Proc. IEEE 2000 Int. Geoscience and Remote Sensing Symp.*, Honolulu, HI, IEEE, 1804–1806, https://doi.org/10.1109/IGARSS.2000.858129.

——, and ——, 2016: A dual-wavelength radar technique to detect hydrometeor phases. *IEEE Trans. Geosci. Remote Sens.*, **54**, 7292–7298, https://doi.org/10.1109/TGRS.2016.2599022.

——, ——, T. Iguchi, and A. Detwiler, 2005: Use of dual-wavelength radar for snow parameter estimates. *J. Atmos. Oceanic Technol.*, **22**, 1494–1506, https://doi.org/10.1175/JTECH1808.1.

Liebe, H. J., T. Manabe, and G. A. Hufford, 1989: Millimeter-wave attenuation and delay rates due to fog/cloud conditions. *IEEE Trans. Antennas Propag.*, **37**, 1612–1617, https://doi.org/10.1109/8.45106.

Mason, S. L., C. J. Chiu, R. J. Hogan, D. Moisseev, and S. Kneifel, 2018: Retrievals of riming and snow density from vertically pointing Doppler radars. *J. Geophys. Res. Atmos.*, **123**, 13 807–13 834, https://doi.org/10.1029/2018JD028603.

Matrosov, S. Y., 1992: Radar reflectivity in snowfall. *IEEE Trans. Geosci. Remote Sens.*, **30**, 454–461, https://doi.org/10.1109/36.142923.

——, 1998: A dual-wavelength radar method to measure snowfall rate. *J. Appl. Meteor.*, **37**, 1510–1521, https://doi.org/10.1175/1520-0450(1998)037<1510:ADWRMT>2.0.CO;2.

McFarquhar, G. M., M. S. Timlin, R. M. Rauber, B. F. Jewett, J. A. Grim, and D. P. Jorgensen, 2007: Vertical variability of cloud hydrometeors in the stratiform region of mesoscale convective systems and bow echoes. *Mon. Wea. Rev.*, **135**, 3405–3428, https://doi.org/10.1175/MWR3444.1.

Meneghini, R., and L. Liao, 2000: Effective dielectric constants of mixed-phase hydrometeors. *J. Atmos. Oceanic Technol.*, **17**, 628–640, https://doi.org/10.1175/1520-0426(2000)017<0628:EDCOMP>2.0.CO;2.

Nguyen, C. M., M. Wolde, A. Battaglia, L. Nichman, N. Bliankinshtein, S. Haimov, K. Bala, and D. Schuettemeyer, 2022: Coincident in situ and triple-frequency radar airborne observations in the Arctic. *Atmos. Meas. Tech.*, **15**, 775–795, https://doi.org/10.5194/amt-15-775-2022.

Ori, D., L. von Terzi, M. Karrer, and S. Kneifel, 2021: SnowScatt 1.0: Consistent model of microphysical and scattering properties of rimed and unrimed snowflakes based on the self-similar Rayleigh–Gans approximation. *Geosci. Model Dev.*, **14**, 1511–1531, https://doi.org/10.5194/gmd-14-1511-2021.

Rauber, R. M., and L. O. Grant, 1987: Supercooled liquid water structure of a shallow orographic cloud system in southern Utah. *J. Appl. Meteor. Climatol.*, **26**, 208–215, https://doi.org/10.1175/1520-0450(1987)026<0208:SLWSOA>2.0.CO;2.

——, and S. W. Nesbitt, 2018: *Radar Meteorology: A First Course.* 1st ed. John Wiley and Sons, 488 pp.

Ryzhkov, A. V., S. E. Giangrande, and T. J. Schuur, 2005: Rainfall estimation with a polarimetric prototype of WSR-88D. *J. Appl. Meteor.*, **44**, 502–515, https://doi.org/10.1175/JAM2213.1.

Tessendorf, S. A., and Coauthors, 2019: A transformational approach to winter orographic weather modification research: The SNOWIE project. *Bull. Amer. Meteor. Soc.*, **100**, 71–92, https://doi.org/10.1175/BAMS-D-17-0152.1.

——, K. Ikeda, C. Weeks, R. Rasmussen, J. Wolff, and L. Xue, 2020: An assessment of winter orographic precipitation and cloud-seeding potential in Wyoming. *J. Appl. Meteor. Climatol.*, **59**, 1217–1238, https://doi.org/10.1175/JAMC-D-19-0219.1.

Thompson, E. J., S. A. Rutledge, B. Dolan, V. Chandrasekar, and B. L. Cheong, 2014: A dual-polarization radar hydrometeor classification algorithm for winter precipitation. *J. Atmos. Oceanic Technol.*, **31**, 1457–1481, https://doi.org/10.1175/JTECH-D-13-00119.1.

Tridon, F., and Coauthors, 2019: The microphysics of stratiform precipitation during OLYMPEX: Compatibility between triple-frequency radar and airborne in situ observations. *J. Geophys. Res. Atmos.*, **124**, 8764–8792, https://doi.org/10.1029/2018JD029858.

Tripp, A., S. Haimov, A. Pazmany, B. Geerts, and J. R. French, 2017: Calibrating the airborne Ka-band precipitation radar aboard the University of Wyoming King Air research aircraft. *38th Radar Meteorology Conf.*, Chicago, IL, Amer. Meteor. Soc., 32, https://ams.confex.com/ams/38RADAR/webprogram/Paper321210.html.

Ulaby, F. T., R. K. Moore, and A. K. Fung, 1981: *Microwave Remote Sensing: Active and Passive.* Vol. 1. Artech House, 456 pp.

University of Wyoming Research Flight Center, 2017a: Flight level data from the University of Wyoming King Air during the Seeded and Natural Orographic Wintertime Clouds—The Idaho Experiment (SNOWIE) project, version 1.0. University of Wyoming Dept. of Atmospheric Science, accessed 15 January 2021, https://doi.org/10.15786/M2MW9F.

——, 2017b: Wyoming Cloud Radar data from the University of Wyoming King Air during the University of Wyoming King Air during the Seeded and Natural Orographic Wintertime Clouds—The Idaho Experiment (SNOWIE) project, version 1.0. University of Wyoming Dept. of Atmospheric Science, accessed 15 January 2021, https://doi.org/10.15786/M2CD4J.

Vali, G., and S. Haimov, 2001: Observed extinction by clouds at 95 GHz. *IEEE Trans. Geosci. Remote Sens.*, **39**, 190–193, https://doi.org/10.1109/36.898682.

Vivekanandan, J., G. Zhang, and M. K. Politovich, 2001: An assessment of droplet size and liquid water content derived from dual-wavelength radar measurements to the application of aircraft icing detection. *J. Atmos. Oceanic Technol.*, **18**, 1787–1798, https://doi.org/10.1175/1520-0426(2001)018<1787:AAODSA>2.0.CO;2.

Wang, Z., G. M. Heymsfield, L. Li, and A. J. Heymsfield, 2005: Retrieving optically thick ice cloud microphysical properties by using airborne dual-wavelength radar measurements. *J. Geophys. Res.*, **110**, D19201, https://doi.org/10.1029/2005JD005969.

——, and Coauthors, 2012: Single aircraft integration of remote sensing and in situ sampling for the study of cloud microphysics and dynamics. *Bull. Amer. Meteor. Soc.*, **93**, 653–668, https://doi.org/10.1175/BAMS-D-11-00044.1.

Weeks, C., 2017: Radiometer data at Horseshoe Bend Site, version 1.0. UCAR/NCAR Earth Observing Laboratory, accessed 17 May 2021, https://doi.org/10.5065/D6VT1QTS.

Wendisch, M., and J.-L. Brenquier, 2013: *Airborne Measurements for Environmental Research: Methods and Instruments*. John Wiley and Sons, 641 pp.

Xue, L., and Coauthors, 2022: Comparison between observed and simulated AgI seeding impacts in a well-observed case from the SNOWIE field program. *J. Appl. Meteor. Climatol.*, **61**, 345–367, https://doi.org/10.1175/JAMC-D-21-0103.1.